

Towards a Practical Use of Sulfide Solid Electrolytes in Solid-State Batteries: Impact of Dry Room Exposure on H₂S Release and Material Properties

Xavier Randrema⁺^[a], Ivan Leteyi Mfiban⁺^[a], Marine Soler,^[a] Irina Profatilova,^{*[a]} Manon Berthault,^[a] Raphael Ramos,^[a] Julien Lavie,^[a] Eric De Vito,^[a] Lionel Blanc,^[a] Sébastien Diry,^[a] Sébastien Launois,^[a] Vasily Tarnopolskiy,^[a] Magali Reytier,^[a] Jean-François Colin,^[a] Céline Barchasz,^[a, b] and Sébastien Liatard^{*[a]}

Sulfide-based solid electrolytes (SEs) are amongst the most promising solid electrolytes for the development of solid-state batteries (SSBs) due to their high ionic conductivity and processing advantage over oxide-based SEs. However, one of the main drawbacks of sulfide SEs is their rapid degradation in presence of humidity. In this study, we investigated the effect of exposing three different sulfide SEs ($\text{Li}_7\text{P}_3\text{S}_{11}$, the argyrodite $\text{Li}_6\text{PS}_5\text{Cl}$ and the chloride-doped argyrodite $\text{Li}_{6-x}\text{PS}_{5-x}\text{Cl}_{1+x}$) to the atmosphere of a dry room at a dew point (DP) = -40°C . For the first time to the best of our knowledge, enhanced infra-red (IR) laser technology was employed to follow and quantify online

and *in-situ* H₂S evolution by the SEs in a dry room environment over 16 h. It was found that argyrodite compounds evolved approximately 8 times less H₂S compared to $\text{Li}_7\text{P}_3\text{S}_{11}$ over 16 h of exposure with peak concentrations between 5 and 16 ppm vol. The exposed materials were studied using X-ray diffraction, Raman spectroscopy, electrochemical impedance spectroscopy, X-ray photoelectron spectrometry (XPS) and galvanostatic cycling. XPS results revealed a formation of Li_2CO_3 on the surface of argyrodite SEs, which served as a robust passivation layer limiting considerably reactions with the dry room atmosphere.

Introduction

Solid-state batteries are considered a promising next generation battery technology due to their potential for increased safety and energy density.^[1] Amongst the solid electrolyte (SE) candidates, sulfide SEs demonstrate the highest ionic conductivity and the most advantageous mechanical properties.^[2] $\text{Li}_7\text{P}_3\text{S}_{11}$ crystalline phase discovered in 2005^[3] and $\text{Li}_6\text{PS}_5\text{Cl}$ argyrodite discovered in 2008^[4] have attracted much interest

due to the ease of synthesis^[5] and high ionic conductivity (17 mScm^{-1} ^[6] and $>24 \text{ mScm}^{-1}$ ^[7] respectively). Good and stable electrochemical performance was obtained in Li-ion batteries containing $\text{Li}_6\text{PS}_5\text{Cl}$ as SE.^[8] Despite all the advantages, there are serious drawbacks impeding a wide commercialization of sulfide SEs. One of the main concern with SEs is their high moisture sensitivity.^[9] The surface of as-synthesized sulfide SEs is modified in contact with air due to fast reactions with humidity. Consequently, the electrochemical performance of SEs is deteriorated and toxic H₂S is released creating safety issues.^[10] This can be potentially the case even for SEs in contact with trace amounts of water contained typically in dry rooms. This feature of sulfide SEs is crucial for the large-scale production process of solid state LIBs since specific high-cost conditions are required to maintain high quality of solid state batteries and safe working environment. In addition, the sensitivity of SEs towards humidity varies as a function of their structure and morphology, therefore adaptation of working environment is necessary. Nevertheless, the problem of humid air sensitivity for SEs has been relatively overlooked in literature compared to other challenges like interfacial electrochemical stability. Moreover, the majority of papers mentioning investigation of air stability of sulfide SEs with quantification of H₂S used closed systems. This kind of measurement setup typically consists of a desiccator under a regulated humid atmosphere (1–60% RH) in which a SE pellet is placed along with one or several H₂S sensors and a fan.^[11] H₂S gas generated by the pellet is spread within the desiccator thanks to the fan and its concentration is measured by H₂S sensors. These setups suffer from serious drawbacks including (i) risks of H₂S concentration

[a] Dr. X. Randrema,⁺ I. Leteyi Mfiban,⁺ Dr. M. Soler, Dr. I. Profatilova, Dr. M. Berthault, Dr. R. Ramos, Dr. J. Lavie, Dr. E. De Vito, L. Blanc, S. Diry, S. Launois, Dr. V. Tarnopolskiy, Dr. M. Reytier, Dr. J.-F. Colin, Dr. C. Barchasz, Dr. S. Liatard
University Grenoble Alpes, CEA, LITEN
38000 Grenoble, France
E-mail: irina.profatilova@cea.fr
sebastien.liatard@cea.fr

[b] Dr. C. Barchasz
Present Address:
Verkor, 1–3 allée du Nanomètre, 38000 Grenoble, France

[+] These authors contributed equally to this work.

[i] Supporting information for this article is available on the WWW under <https://doi.org/10.1002/batt.202300380>

This publication is part of a joint Special Collection on Solid State Batteries, featuring contributions published in Advanced Energy Materials, Energy Technology, Batteries & Supercaps, ChemSusChem, and Advanced Energy and Sustainability Research.

© 2023 The Authors. Batteries & Supercaps published by Wiley-VCH GmbH. This is an open access article under the terms of the Creative Commons Attribution Non-Commercial NoDerivs License, which permits use and distribution in any medium, provided the original work is properly cited, the use is non-commercial and no modifications or adaptations are made.

overestimation due to relatively small volumes of desiccators, (ii) position-dependent measurements of H₂S concentrations leading to reproducibility issues, (iii) difficulties to directly use SE powders for measurements and (iv) loss of initial measurement data due to the necessary set-up and system equilibration delay. In addition, portable H₂S sensors used for measurements in closed systems have limitations in terms of frequency of data acquisition, nature of the carrier gas, cross-sensitivity with other molecules like organic solvents and requirements of relative humidity levels between 5 and 95 % to work correctly.^[12] Hence, there is a need for a more precise and representative methods to characterize gas evolution from SEs reactions with traces of moisture in real-life conditions.

It should be mentioned that a majority of the studies on solid state LIBs with sulfide SEs^[13] were designed for lab scale only, meaning low energy densities and inappropriate assembling process for mass production. To match current production lines, solid state LIBs should be manufactured in a dry room, using roll-to-roll processes.^[14] An example of solid state battery prototype was described in the work of Nam et al.^[15] demonstrating high energy density (184 Wh kg⁻¹). However, the prototype assembly was conducted in an argon-filled dry box with H₂O < 1 ppm.

In this work, we evaluate the dry-room air stability of in-house synthesized Li₇P₃S₁₁ and chlorine-doped argyrodite SEs along with commercial Li₆PS₅Cl in conditions close to large-scale solid state batteries production. A highly sensitive and precise flow-through setup for H₂S quantification was designed to characterize *in-situ* gas evolution by the SEs upon exposure to a dry room atmosphere with a dew point (DP) of -40 °C. The use of enhanced IR laser technology based on Optical Feedback Cavity Enhanced Absorption Spectroscopy (OFCEAS) principle allowed overcoming the drawbacks of portable H₂S sensors typically used for investigation of SEs. To the best of our knowledge, this is the first contribution reporting a use of online OFCEAS gas analyzer for characterization of sulfide-based SEs for LIBs in a real dry room environment. Dynamics of H₂S generation by SEs exposed to dry room atmosphere was

studied over 16 h. The properties of the exposed SEs were further investigated using X-ray diffraction (XRD), Raman spectroscopy, Electrochemical Impedance Spectroscopy (EIS), Scanning Electron Microscopy (SEM) and X-ray Photoelectron Spectroscopy (XPS), showing the evidence of an efficient passivation layer formation on the surface of argyrodite powders. Finally, galvanostatic cycling was compared for the LIBs containing SEs before and after the exposure to dry room atmosphere using in-house solid state battery test setup.

Results and Discussion

Synthesis and characterization of pristine sulfides

Sulfide electrolyte Li₇P₃S₁₁ (Li₇P₃S₁₁-Pri) was synthesized in the conditions previously described and adapted from Busche et al.^[16] The details of the synthesis are included in the experimental section. The profile matching of Li₇P₃S₁₁-Pri is shown in Figure 1 and ascertains the synthesis of Li₇P₃S₁₁ material. As expected, Li₇P₃S₁₁-Pri sample is crystallized in P-1 space group^[17] with the lattice parameters $a = 12.5039$ (6) Å, $b = 6.0277$ (4) Å and $c = 12.5218$ (6) Å. Raman spectroscopy corroborated the material identification. The Raman spectrum showed the two main characteristic bands of Li₇P₃S₁₁. These 2 bands are typically attributed to *ortho*-thiophosphate (PS₄³⁻) and *pyro*-thiodiphosphate (P₂S₇⁴⁻) units, respectively centered at 421 cm⁻¹ and 405 cm⁻¹ (Figure 1b).^[18]

The synthesis of chlorine-doped Li_{6-x}PS_{5-x}Cl_{1+x} was inspired and adapted from Adeli et al.^[19] The details of the procedure are described in the experimental section. Figure S1 presents the Raman spectrum of the as-synthesized Cl-doped argyrodite. The main band visible around 428 cm⁻¹ attests of the presence of the PS₄³⁻ units, which are isolated units in the face-centered cubic argyrodite structure. Figure 2(a) displays the XRD profile matching conducted according to the argyrodite F-43 m space group.^[4] In addition to the argyrodite structure, the diffractogram also shows the presence of small quantities of the LiCl

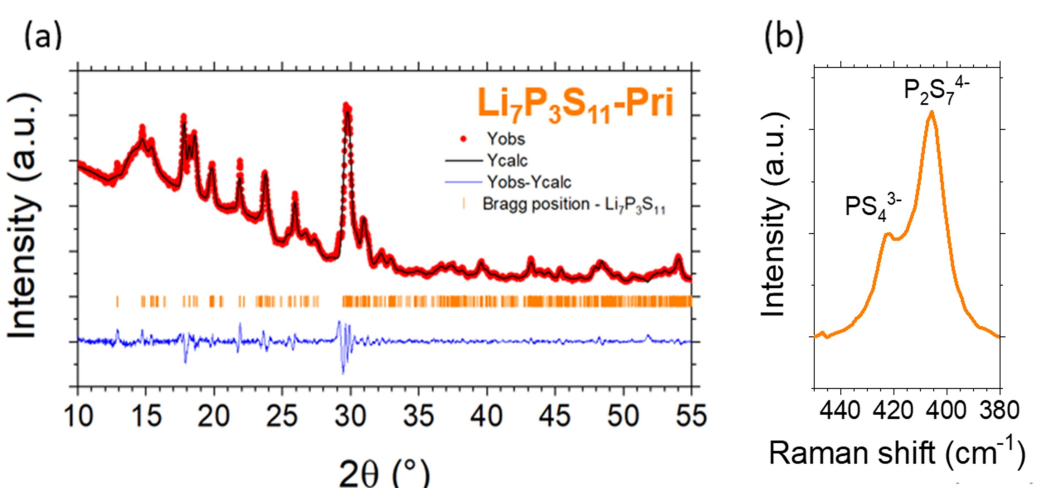


Figure 1. XRD characterization of Li₇P₃S₁₁-Pri sample with a) the profile matching and b) the Raman spectrum in the thiophosphate area.

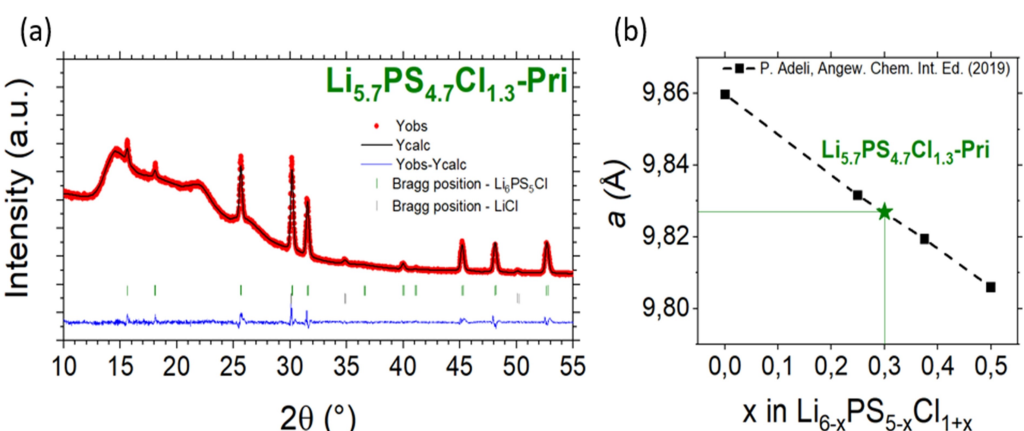


Figure 2. XRD characterization of chlorine-doped $\text{Li}_{6-x}\text{PS}_{5-x}\text{Cl}_{1+x}$ sample with a) the profile matching and b) the comparison to reference^[19] that suggests $\text{Li}_{5.7}\text{PS}_{4.7}\text{Cl}_{1.3}$ -Pri as the resulting stoichiometry.

precursor (Fm-3 m space group^[20]) at $2\theta = 34.8^\circ$ and $2\theta = 50.1^\circ$. The respective lattice parameters are $a = 9.8272$ (3) Å and $a = 5.1492$ (4). To estimate the stoichiometry of our Cl-doped argyrodite material, its extracted lattice parameter a was compared to the lattice parameters obtained by Adeli et al. and the result is presented in Figure 2(b). This comparison seems to indicate that our synthesis did not yield the targeted stoichiometry of $\text{Li}_{5.5}\text{PS}_{4.5}\text{Cl}_{1.5}$. The lattice parameter from our product is higher than reported by Adeli et al. for a $\text{Li}_{5.5}\text{PS}_{4.5}\text{Cl}_{1.5}$ and would then correspond approximately to the $\text{Li}_{5.7}\text{PS}_{4.7}\text{Cl}_{1.3}$ stoichiometry. Moreover, LiCl residues observed in the diffractogram in Figure 2, attest an incomplete reaction and a lack of chlorine in the final electrolyte structure. To corroborate this stoichiometry estimation, a ^{31}P NMR experiment was conducted (Figure S2). Three contributions were found (P1, P2 and P3) to fit the phosphorous peak. When compared to the findings of Feng et al.,^[21] the deconvolution of the peak should correspond to a $\text{Li}_{5.5}\text{PS}_{4.5}\text{Cl}_{1.5}$ stoichiometry. These results lead us to conclude that the stoichiometry of our chlorine-doped argyrodite sample is $\text{Li}_{6-x}\text{PS}_{5-x}\text{Cl}_{1+x}$ with $0.3 \leq x < 0.5$. It will be labelled $\text{Li}_{5.7}\text{PS}_{4.7}\text{Cl}_{1.3}$ -Pri for the remaining of the paper.

H₂S release by the SEs

The dynamics of H₂S formation were observed for static SE powders exposed to a dry room atmosphere with a DP of -40°C over a duration of 16 h. The amounts of H₂S released in these conditions were quantified and compared for each SE. A homemade flow-through gas measurement setup was used, as shown in Figure 3(a). H₂S and SO₂ were monitored *in-situ* online with lower limits of detection (LLODs) of 1 ppb and 5 ppb (vol), respectively, which ensured very high sensitivity of measurements. However, SO₂ was not detected for any of the investigated SEs. The details of measurement procedure are given in the experimental section. The gas measurements were conducted continuously before and after the SE powder pouring into the gas washing bottle without any data loss. The flow-through setup is more representative of a practical SEs

handling situation in a dry room line unlike conventional closed setups mentioned in the introduction. In fact, concentration overestimation is less likely to occur in a flow-through system, where produced gases are pumped-out from a reaction interface. To the best of our knowledge, only few publications^[22] mention flow-through-type gas measurement setups for the study of moisture-exposed solid electrolytes for batteries and this is the first report on using enhanced IR OFCEAS technology for this kind of *in-situ* measurements.

Figure 3(b, c) compares the dynamics of H₂S evolution for 1 g of $\text{Li}_7\text{P}_3\text{S}_{11}$ -Pri, 1 g of $\text{Li}_{5.7}\text{PS}_{4.7}\text{Cl}_{1.3}$ -Pri and 1 g of $\text{Li}_6\text{PS}_5\text{Cl}$ -Pri during a long-term dry room atmosphere exposure. The amount of powder was selected to match a previous prototyping study where the cell was composed of approximately 1.2 g of $\text{Li}_6\text{PS}_5\text{Cl}$ in a complete monolayer pouch cell ($80 \times 60 \text{ mm}^2$).^[15] Two types of H₂S evolution profiles were observed: (i) growth of H₂S concentration during 1 h with subsequent stabilization at around 2.5 ppm vol. for the rest of the test in the case of $\text{Li}_7\text{P}_3\text{S}_{11}$ and (ii) a sharp H₂S peak formed during 1 h followed by a stabilization at sub-ppm values (<0.3 ppm vol.) for $\text{Li}_{5.7}\text{PS}_{4.7}\text{Cl}_{1.3}$ -Pri and $\text{Li}_6\text{PS}_5\text{Cl}$ -Pri. This peak is ascribed to surface reaction of SEs grains and the plateau likely corresponds to diffusion-controlled reaction of the bulk of SE powders. There is an ongoing work to confirm this hypothesis by our group, which will be a matter of a separate publication. According to the results above, it appears that all the three investigated SEs demonstrate reaction with trace humidity, which is confirmed by H₂S evolution. The surface reactions are mostly completed after approximately 2 h of the exposure test in Figure 3(b) followed by a stabilization of H₂S concentration at different levels for the three SEs. It seems that there is an efficient passivation for both argyrodite compounds after 2 h of exposing since further H₂S evolution rates are extremely low. It is likely that the degradation products formed via reaction with atmosphere on the surface of $\text{Li}_{5.7}\text{PS}_{4.7}\text{Cl}_{1.3}$ -Pri and $\text{Li}_6\text{PS}_5\text{Cl}$ -Pri serve as a barrier against further humidity penetration to the bulk of the samples. However, $\text{Li}_7\text{P}_3\text{S}_{11}$ -Pri in dry room conditions do not form a robust passivation layer on its surface, as evidenced by the elevated H₂S evolution rate for this powder

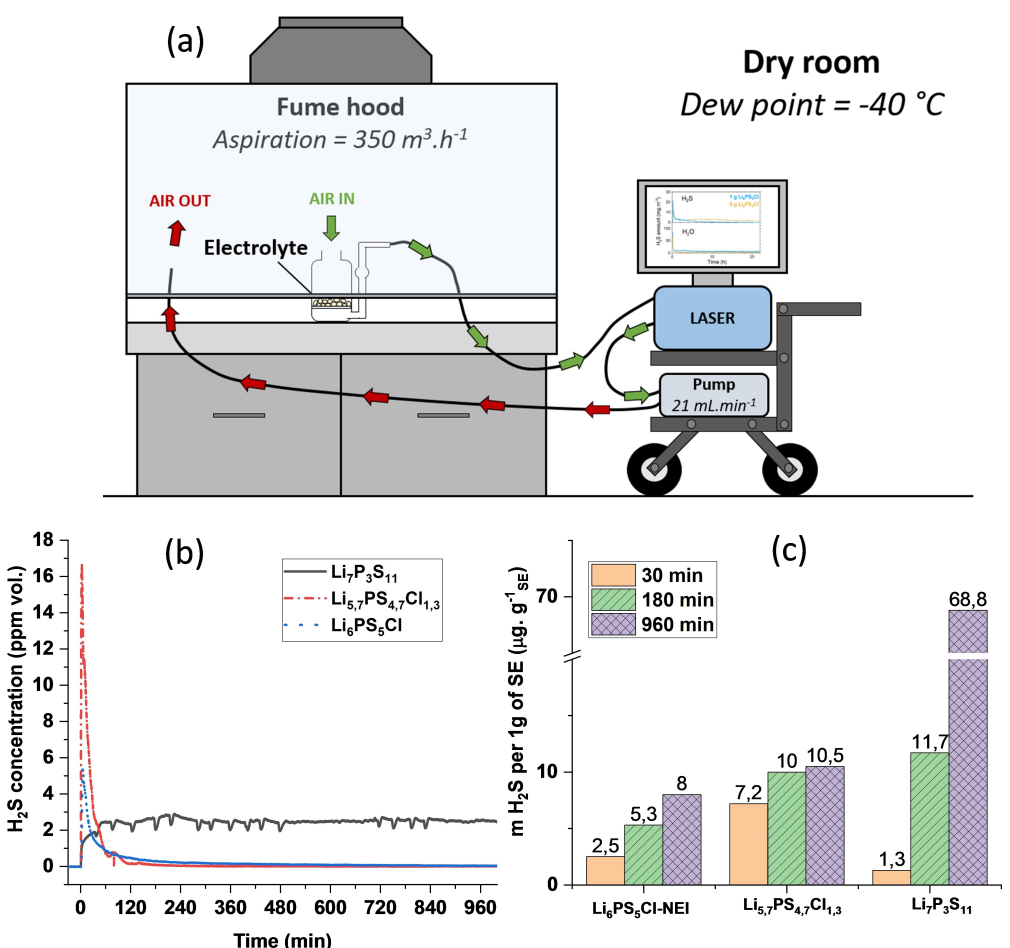


Figure 3. Schematic of the gas measurement setup used to investigate moisture sensitivity of SEs under a laboratory fume hood in a dry room ($\text{DP} = -40^\circ\text{C}$) consisting of a gas washing bottle of 350 cm^3 volume connected to OFCEAS gas analyzer. a) 1 g of the SE powder was placed onto coarse fritted disc inside the gas washing bottle; b) H_2S evolution profiles for $\text{Li}_7\text{P}_3\text{S}_{11}\text{-Pri}$ (solid line), $\text{Li}_{5.7}\text{PS}_{4.7}\text{Cl}_{1.3}\text{-Pri}$ (dash dot line) and $\text{Li}_6\text{PS}_5\text{Cl}\text{-Pri}$ (short dash line) obtained during a dry room atmosphere exposure; c) H_2S quantities evolved by the three investigated SEs over 30, 180 and 960 min.

during 16 h in Figure 3(b). The possible reasons are different nature or morphology of degradation products compared to the case of argyrodite powders. Similar types of H_2S evolution profiles were obtained by Lu et al.^[22b] for Li_3PS_4 using a flow-through setup. However, a quantitative comparison of the results is not possible due to important differences in test conditions (N_2 carrier gas, relative humidity 100%, exposing of SEs during 300 min).^[22b]

Figure 3(c) shows the total H_2S amounts integrated over 30, 180 and 960 min in Figure 3(b). Short term exposure time (30 min) leads to a lower H_2S quantity for $\text{Li}_7\text{P}_3\text{S}_{11}\text{-Pri}$ ($1.3 \mu\text{g g}^{-1}\text{SE}$) compared to argyrodite materials (7.2 and $2.5 \mu\text{g g}^{-1}\text{SE}$ for $\text{Li}_{5.7}\text{PS}_{4.7}\text{Cl}_{1.3}\text{-Pri}$ and $\text{Li}_6\text{PS}_5\text{Cl}\text{-Pri}$, respectively). When considering a longer exposure time, the trend is reversed, in accordance with H_2S formation profiles depicted in Figure 3(b). As was mentioned above, $\text{Li}_{5.7}\text{PS}_{4.7}\text{Cl}_{1.3}\text{-Pri}$ and $\text{Li}_6\text{PS}_5\text{Cl}\text{-Pri}$ demonstrate a rapid H_2S productive surface reaction followed by an efficient passivation that probably hinders water and CO_2 molecules diffusion through SE grains. Finally, the total H_2S amount generated by $\text{Li}_7\text{P}_3\text{S}_{11}\text{-Pri}$ over 16 h was $68.8 \mu\text{g g}^{-1}\text{SE}$ while $\text{Li}_{5.7}\text{PS}_{4.7}\text{Cl}_{1.3}\text{-Pri}$ and $\text{Li}_6\text{PS}_5\text{Cl}\text{-Pri}$ produced only 10.5 and

$8 \mu\text{g g}^{-1}\text{SE}$, respectively, Figure 3(c). After the dry room exposure experiment, the powders were sealed in a glove box under argon and named $\text{Li}_7\text{P}_3\text{S}_{11}\text{-Exp}$, $\text{Li}_{5.7}\text{PS}_{4.7}\text{Cl}_{1.3}\text{-Exp}$ and $\text{Li}_6\text{PS}_5\text{Cl}\text{-Exp}$.

Although there is a clear dependence of the reactivity on the chemical composition, it is necessary to exercise caution comparing the absolute quantities of evolved H_2S , which is a product of hydrolysis of $\text{Li}_7\text{P}_3\text{S}_{11}$ and $\text{Li}_{6-x}\text{PS}_{5-x}\text{Cl}_{1+x}$. The hydrolysis reaction rates are impacted by the chemical composition of the SE and also by other parameters such as particle size distribution and specific surface area of a SE, as highlighted recently by Singer et al.^[12] SEM data with estimation of particle size for the SEs can be found in Figure S3. The Figure shows that particles size distribution of $\text{Li}_7\text{P}_3\text{S}_{11}\text{-Pri}$ and $\text{Li}_6\text{PS}_5\text{Cl}\text{-Pri}$ are quite similar and consists mostly of small particles under $10 \mu\text{m}$, whereas $\text{Li}_{5.7}\text{PS}_{4.7}\text{Cl}_{1.3}\text{-Pri}$ has a non-negligible amount of particles above $20 \mu\text{m}$. Despite the difference in particle size distribution, the shapes for H_2S evolution profiles are similar for both argyrodite materials in Figure 3(b). Therefore, we believe that the H_2S evolution trends are mostly impacted by the

chemical composition of the SE powders in this study since measurement conditions are similar for all the samples.

In addition, it is important to bear in mind that the results obtained pertain to static powders in a controlled dew point environment, and where the detection is in close proximity to the H₂S emission source. The actual handling of SSEs (mixing/manipulations) combined with moisture level fluctuations (variation of the number of operators in a dry room close to SEs or non-stable dew point regulation) could be other sources that influence the dynamics of H₂S emissions. The European directives fixed the H₂S time-weighted average (TWA) based on an 8-hour workday at 5 ppm and the short term exposure limit (STEL) at 10 ppm.^[23] In our study, at a given flow rate, the Cl-doped argyrodite is the only one that exceeds these values (Figure 3b), and only during the initial peak. Overall, we think the three sulfides studied herein should be handled under a fume hood or any equally effective extraction or filtration equipment, even in a dry room environment. Future studies in our laboratories will reveal how a dryer environment (DP < -40 °C) reduces H₂S generation.

SEs properties after exposure

The XRD patterns of Pristine and Exposed samples are shown in Figure 4(a). The exposure to the dry room atmosphere did not seem to extensively affect the crystal structure of the compounds. The main reflections for Li₇P₃S₁₁-Exp, Li_{5,7}PS_{4,7}Cl_{1,3}-Exp and Li₆PS₅Cl-Exp did not change when compared to their pristine counterparts. However, further analysis was performed by running a profile matching analysis on each sample, allowing for the extraction of the lattice parameters (Figure S4 and Table S1). According to these results, both in-house and commercial argyrodite compounds were not impacted by the dry room moisture (from $a_{\text{pri}} = 9.8272(3)$ to $a_{\text{exp}} = 9.8293(3)$ Å for Li_{5,7}PS_{4,7}Cl_{1,3} samples and from $a_{\text{pri}} = 9.8489(2)$ to $a_{\text{exp}} = 9.8471(3)$ Å for Li₆PS₅Cl samples). Measurable changes were observed in the case of Li₇P₃S₁₁ samples (Figure 4b) especially for a and c

lattice parameters (from $a_{\text{pri}} = 12.5039(6)$ to $a_{\text{exp}} = 12.5137(10)$ Å and from $c_{\text{pri}} = 12.5218(6)$ to $c_{\text{exp}} = 12.5127(13)$ Å) suggesting a small effect of the exposure to the dry room atmosphere on the crystal structure.

The Raman spectra of pristine and exposed samples are shown in Figure 5(a). Firstly, one should note the small shift observed between Li_{5,7}PS_{4,7}Cl_{1,3} and Li₆PS₅Cl samples, with a main band centered around 426 cm⁻¹ for commercial argyrodite, and at 429 cm⁻¹ for the chlorine-doped product.^[24] We believe that this change is due to the chlorine-rich environment, which strengthens atom interactions due to higher electronegativity, leading to a signal shift towards higher energy. When comparing pristine and exposed samples, no peak shift was observed for any of the sulfide SEs. However, for both Li₆PS₅Cl-Exp and Li_{5,7}PS_{4,7}Cl_{1,3}-Exp samples, a shoulder centered at 419 cm⁻¹ appears on the main thiophosphate peak. It corresponds to a maximum of 5% of the total band surface area (Figure 5b). This band is more easily observed when argyrodite materials are exposed to ambient air and is attributed to the formation of oxysulfides.^[25] In our experiment, this suggests that some of the sulfur atoms in both argyrodite materials are replaced by oxygen atoms to form oxysulfides upon exposure to the dry room atmosphere. No observable changes in the Raman signal were observed for Li₇P₃S₁₁ samples. It should be noted than we cannot rule out the minute formation of oxysulfides in Li₇P₃S₁₁ due to the overlapping contribution from P₂S₇⁴⁻ units.

In order to further understand the effect of the hydrolysis reaction on the Raman spectra, a controlled exposure experiment to normal lab atmosphere was performed through a leak valve while tracking Raman spectra evolution (Figure S5). In the case of Li₇P₃S₁₁-Pri, a clear extinction of the P₂S₇⁴⁻ band is visible along with the formation of thiol bonds (SH) at 2545 cm⁻¹. For Li₆PS₅Cl-Pri sample, the band of PS₄³⁻ slightly decreases in favor of the PSO_x band centered at 419 cm⁻¹ and SH bonds are also visible. These results corroborate the findings of Muramatsu et al.^[10] supporting the hypothesis of a hydrolysis mechanism

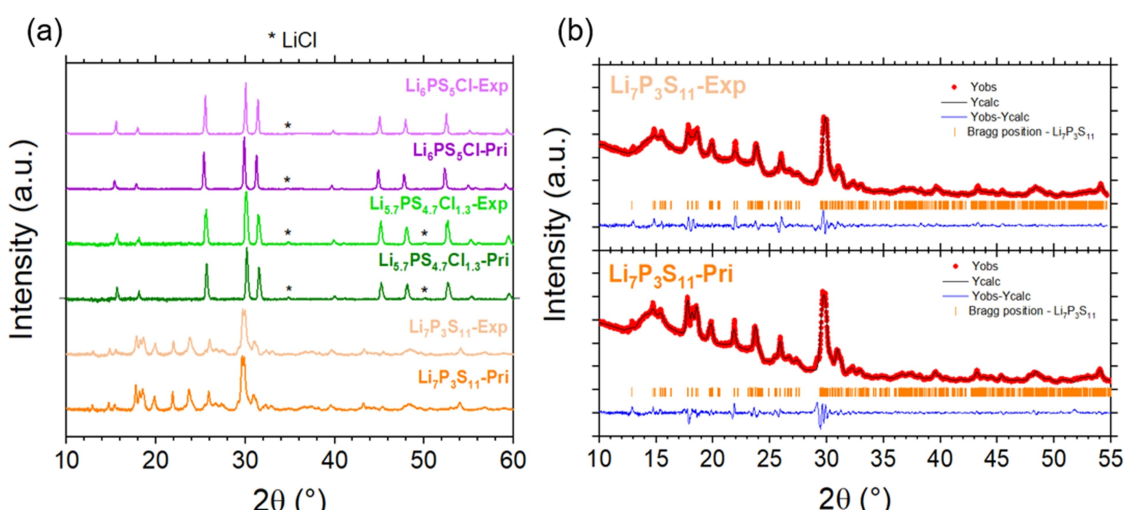


Figure 4. a) XRD patterns of pristine and exposed samples. b) Profile matching of both Li₇P₃S₁₁ samples.

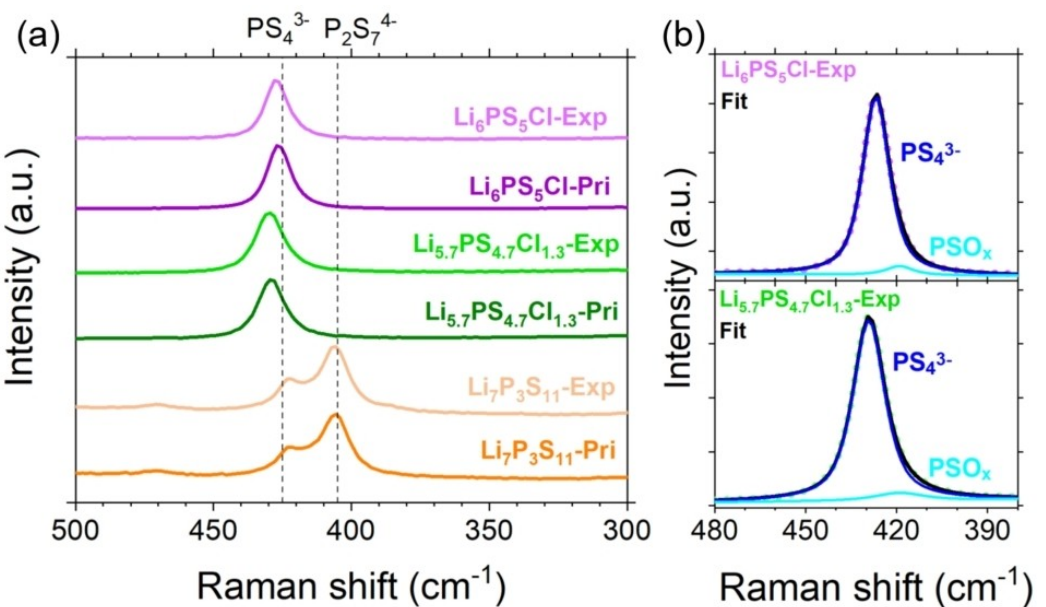


Figure 5. a) Raman spectra of pristine and exposed samples in the thiophosphate area with Li₇P₃S₁₁-Pri (dark orange), Li₇P₃S₁₁-Exp (light orange), Li_{5.7}PS_{4.7}Cl_{1.3}-Pri (dark green), Li_{5.7}PS_{4.7}Cl_{1.3}-Exp (light green), Li₆PS₅Cl-Pri (dark purple), Li₆PS₅Cl-Exp (light purple). b) highlight of a 2nd contribution for argyrodite materials, attributed to PSO_x (light blue) after dry room atmosphere exposing. The results of fitting are in black.

involving thiol and PSO_x formation, as well as indicating a greater sensitivity of P₂S₇⁴⁻ units to moisture.

XPS spectra of Cl 2p, C1s, O 1s and Li 1s, S 2p, P 2p orbitals are shown in Figures 6(a) and S6, respectively, and confirm the products identification based on XRD and Raman, namely Li₇P₃S₁₁ and two argyrodite materials. The same signals are visible for Li_{5.7}PS_{4.7}Cl_{1.3} and Li₆PS₅Cl samples in the case of S, P and Cl, revealing the argyrodite environment by means of the 2p_{3/2}-2p_{1/2} doublet presence for respectively 162 eV (S 2p), 132.5 eV (P 2p) and 198.8 eV (Cl 2p).^[26]

Figure 6(b, c), presenting the XPS C 1s and O 1s spectra, underline the major differences appearing between Li_{5.7}PS_{4.7}Cl_{1.3}-Pri and Li_{5.7}PS_{4.7}Cl_{1.3}-Exp samples on one hand, and between Li₆PS₅Cl-Pri and Li₆PS₅Cl-Exp samples on the other hand. Additional contributions are indeed observed in the case of both exposed samples at 290 eV (C 1s) and 531.7 eV (O 1s). The combination of those peaks is well known and identified as chemical environments typically found in carbonate-based compounds.^[27] This also explains the relative intensity increase observed in O 1s spectra. The lower intensity peaks observed on C 1s spectra for both pristine argyrodite materials are probably due to surface contamination by adsorption of carbon-based organic molecules. These peaks can also be related to the O 1s spectra, which are also lower in intensity and are their counterpart. Besides, the carbonates surface enrichment gives rise to the higher XPS intensity observed on both exposed argyrodites samples, untangling the intensity increase of all peaks and in particular, the one located at 290 eV and related to carbonates groups. It appears that both argyrodites reacted with the dry room atmosphere to generate these carbonate-based surface products. Chen et al. also observed the formation of carbonates on Li₆PS₅Cl when

exposed to dry room atmosphere for 24 h.^[25] On the contrary, these contributions are either not present, or in low intensity, meaning that Li₂CO₃ is not present at the surface of Li₇P₃S₁₁-Exp sample. This is confirmed by the overall shapes of both C 1s and O 1s spectra, which is quite similar for Li₇P₃S₁₁ exposed and pristine samples. It seems that XPS spectroscopy is not suitable to clearly observe the degradation products of Li₇P₃S₁₁-Exp due to interferences of bonds energies with a pristine material. According to the profile of degassed H₂S presented in Figure 3, we suggest that a passivation layer based on Li₂CO₃ is formed for both argyrodite materials leading to a peak of H₂S followed by its rapid decrease. In the case of Li₇P₃S₁₁-Exp sample, the degradation products do not form an efficient passivation layer leading to the continuous H₂S release.

Figure 7(a) presents the Nyquist plot of both pristine and exposed samples for each sulfide SE. In the case of both Li₇P₃S₁₁ and Li₆PS₅Cl samples, a part of a semi-circle is observed at high frequencies, which is attributed to the total solid electrolyte lithium ion conduction. The spectra were fitted using an equivalent circuit based on an initial resistor R₀ (for the device and current collectors resistance), in series with another resistor R₁ (for solid electrolyte resistance), in parallel with a constant phase element CPE₁ (for the non-ideal capacitance between particles) and in series with another constant phase element (for the impedance of both top and bottom electrode-electrode junctions). In the case of Li_{5.7}PS_{4.7}Cl_{1.3} samples, ionic conductivity is higher and only Warburg impedance signal is distinguished, leading to an equivalent circuit based on an initial resistor R₀ and a CPE only. The ionic conductivity, σ, was calculated from the following equation:

$$\sigma = \frac{1}{R_0 + R_1} \times \frac{t}{A} \quad (1)$$

in which A is the pellet surface area and t is the pellet thickness. Detailed parameters of the fit are available in Table S2. Figure 7(b) shows the resulting ionic conductivities extracted from the fitted Nyquist plot. Notably, the $\text{Li}_{5.7}\text{PS}_{4.7}\text{Cl}_{1.3}$ samples demonstrate a substantial enhancement in ionic conductivity, highlighting the advantageous influence of chlorine-doped stoichiometry. This improvement can be attributed to the greater disorder created by the interchangeability between Cl^- and S^{2-} on Wyckoff 4a and 4d positions.^[28] For all samples, pristine and exposed conductivity values are very close. $\text{Li}_7\text{P}_3\text{S}_{11}$ -Pri and $\text{Li}_7\text{P}_3\text{S}_{11}$ -Exp samples exhibit 0.74 and 0.72 mS cm^{-1} ,

respectively, $\text{Li}_{5.7}\text{PS}_{4.7}\text{Cl}_{1.3}$ -Pri and $\text{Li}_{5.7}\text{PS}_{4.7}\text{Cl}_{1.3}$ -Exp samples show 4.95 and 4.92 mS cm^{-1} and $\text{Li}_6\text{PS}_5\text{Cl}$ -Pri and $\text{Li}_6\text{PS}_5\text{Cl}$ -Exp samples present 1.22 and 1.24 mS cm^{-1} . Thus, despite the minor changes observed in XRD, XPS and Raman spectroscopy accompanied by H_2S release for the exposed samples, the dry room atmosphere had no discernible impact on the ionic conductivity of the three types of SEs.

Finally, SSBs were assembled using both pristine and exposed SEs to evaluate the impact of dry room exposure on the electrochemical performance of LiIn/NMC cells. The electrochemical tests were conducted at room temperature and C/20 between 2.0–3.7 V vs. $\text{Li}_{0.38}\text{In}_{0.62}$. To assess the reproducibility of the test, three cells were fabricated for each sample. A detailed description of the cell fabrication steps is available in the experimental section.

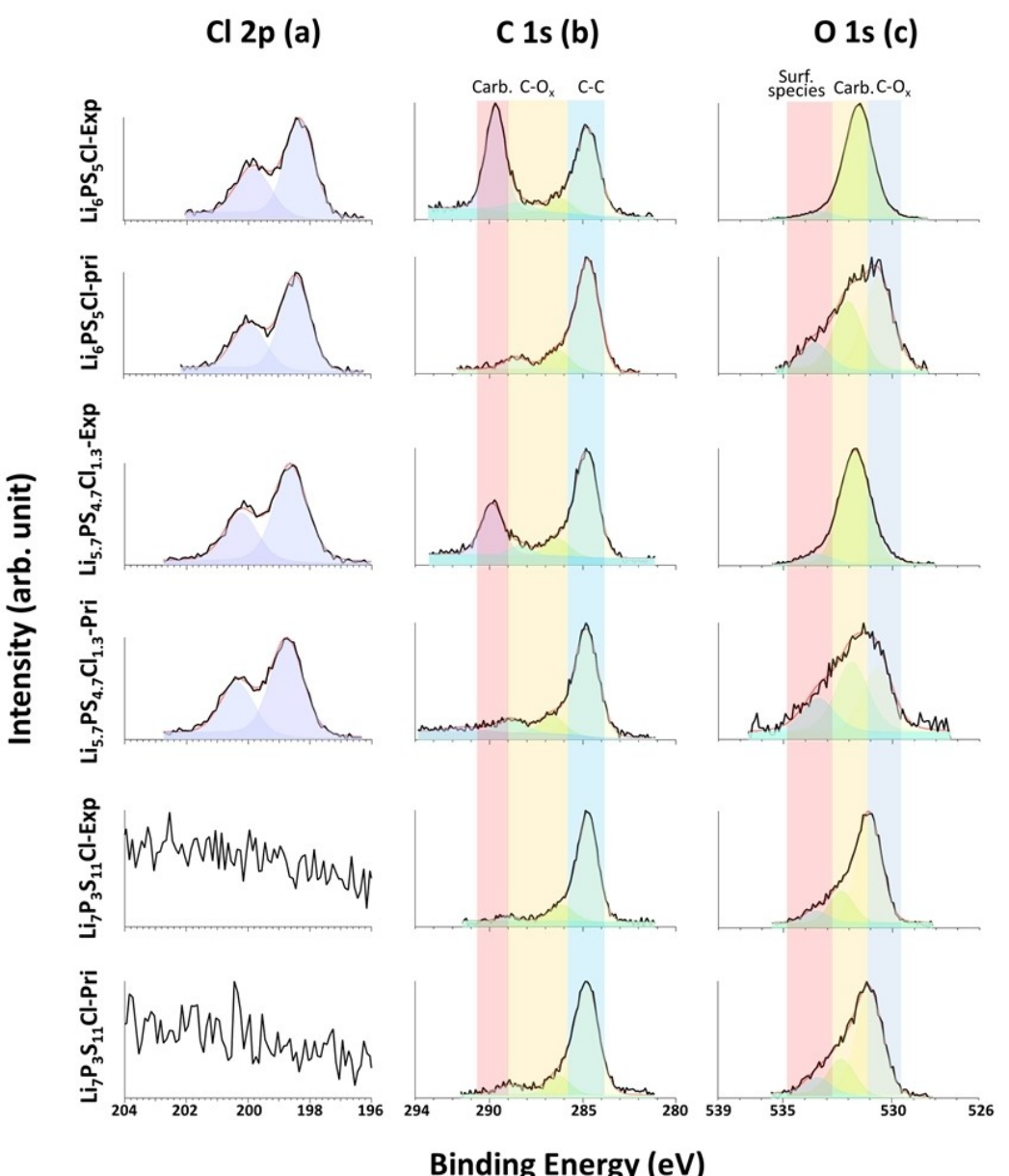


Figure 6. a) XPS results of pristine and exposed samples with Cl 2p spectra. b) C 1s spectra and c) O 1s spectra for $\text{Li}_7\text{P}_3\text{S}_{11}$, $\text{Li}_{5.7}\text{PS}_{4.7}\text{Cl}_{1.3}$ and $\text{Li}_6\text{PS}_5\text{Cl}$.

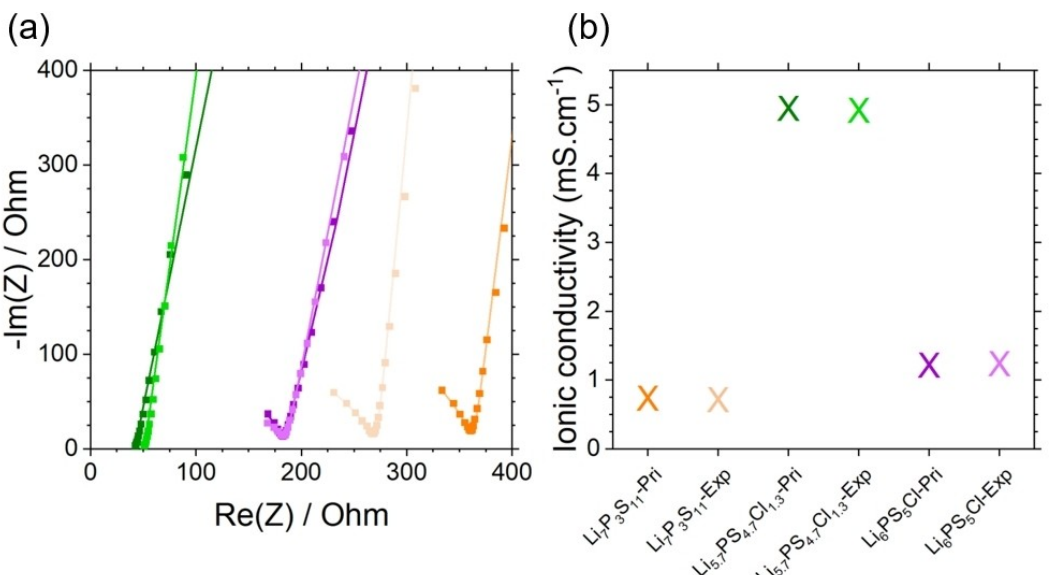


Figure 7. a) Nyquist plot of pristine and exposed samples with the experimental (square dots) and the fitted data (straight lines). b) Resulting ionic conductivity extracted from the fit. $\text{Li}_7\text{P}_3\text{S}_{11}\text{-Pri}$ (dark orange), $\text{Li}_7\text{P}_3\text{S}_{11}\text{-Exp}$ (light orange), $\text{Li}_{5.7}\text{PS}_{4.7}\text{Cl}_{1.3}\text{-Pri}$ (dark green), $\text{Li}_{5.7}\text{PS}_{4.7}\text{Cl}_{1.3}\text{-Exp}$ (light green), $\text{Li}_6\text{PS}_5\text{Cl}\text{-Pri}$ (dark purple), $\text{Li}_6\text{PS}_5\text{Cl}\text{-Exp}$ (light purple).

Figure 8(a–c) displays the voltage profiles obtained during the first cycle for all 3 cells per sample. The charge and discharge capacities of both $\text{Li}_7\text{P}_3\text{S}_{11}$ samples are notably low ($< 50 \text{ mAh g}^{-1}$), and the reproducibility between the cells is relatively poor. Results obtained previously by Calpa et al.^[29] showed that when used in the cathode composition, the morphology of the particles of $\text{Li}_7\text{P}_3\text{S}_{11}$ is key for this electrolyte to function. In this study, we did not attempt to optimize the particle size for our cell configuration and used the same electrolyte in both the cathode and the separating layer. Upon cycling, all cells with $\text{Li}_7\text{P}_3\text{S}_{11}$ lost most of their capacity within a few cycles (Figure 8d). No significant difference was observed between cells with $\text{Li}_7\text{P}_3\text{S}_{11}\text{-Pri}$ and cells with $\text{Li}_7\text{P}_3\text{S}_{11}\text{-Exp}$. The dominant effect being the poor performance of the cells, it is not possible to conclude on the effect of dry room exposure on electrochemical performance for this electrolyte.

Cells containing argyrodite materials $\text{Li}_6\text{PS}_5\text{Cl}$ and $\text{Li}_{5.7}\text{PS}_{4.7}\text{Cl}_{1.3}$ performed better. Initial discharge capacities were $114 \pm 9 \text{ mAh g}^{-1}$ for $\text{Li}_{5.7}\text{PS}_{4.7}\text{Cl}_{1.3}\text{-Pri}$ and $107 \pm 6 \text{ mAh g}^{-1}$ for $\text{Li}_{5.7}\text{PS}_{4.7}\text{Cl}_{1.3}\text{-Exp}$. In this particular case, the dry room exposure leads to a decrease in capacity accompanied with a narrower dispersion of the results. The cycling results for the chloride-doped electrolyte showed a better initial coulombic efficiency (ICE) for the exposed sample, but the rate of capacity fade is very similar between the pristine and exposed samples. The exposition to the dry room atmosphere and the minor modifications that occurred at the surface of the powder could be the source of these small changes in electrochemical behavior.

The commercial argyrodite performed the best in terms of capacity and reproducibility with initial discharge capacities averaging $138 \pm 4 \text{ mAh g}^{-1}$ for $\text{Li}_6\text{PS}_5\text{Cl}\text{-Pri}$ and $135 \pm 4 \text{ mAh g}^{-1}$ for $\text{Li}_6\text{PS}_5\text{Cl}\text{-Exp}$. The highest ICE value was 70%. Improved ICE

values can be found in the literature for this type of system, generally thanks to a protective coating on the NMC particles that prevents excessive reactivity with the sulfide SEs.^[30] The commercial NMC used for this study was not optimized for use with sulfide electrolytes. This leads to a large initial charge capacity corresponding to the oxidation of the NMC and of parts of the sulfide electrolyte in contact with NMC or carbon material as previously demonstrated by Auvergniot et al.^[31] Furthermore, it seems that the dry room exposure has affected slightly the cycling stability of $\text{Li}_6\text{PS}_5\text{Cl}$.

Overall, for $\text{Li}_7\text{P}_3\text{S}_{11}$, the conditions of this electrochemical test did not allow us to conclude on the influence of the dry room exposure on electrochemical performance. In the case of $\text{Li}_{5.7}\text{PS}_{4.7}\text{Cl}_{1.3}$, its intrinsic instability due to the presence of excess chlorine did not lead to optimal capacity. It looked like the Li_2CO_3 layer formed on its surface after exposure had a small beneficial effect on electrochemical performance. Finally, in the case of the commercial argyrodite $\text{Li}_6\text{PS}_5\text{Cl}$, the dry room exposure seemed to have a small detrimental effect on the cycling stability of the cells. However, this study should not prevent further work on the fabrication of sulfide-based SSBs in dry room environments. Many parameters in a production environment would differ from our study and could lead to different results. Previous work from Chen et al.^[25] showed that SE exposure to dry room air did not impact SSB performance, and this difference in results could be explained by differences in test cell configuration, experimental conditions during exposing or particle size distribution of the electrolyte.

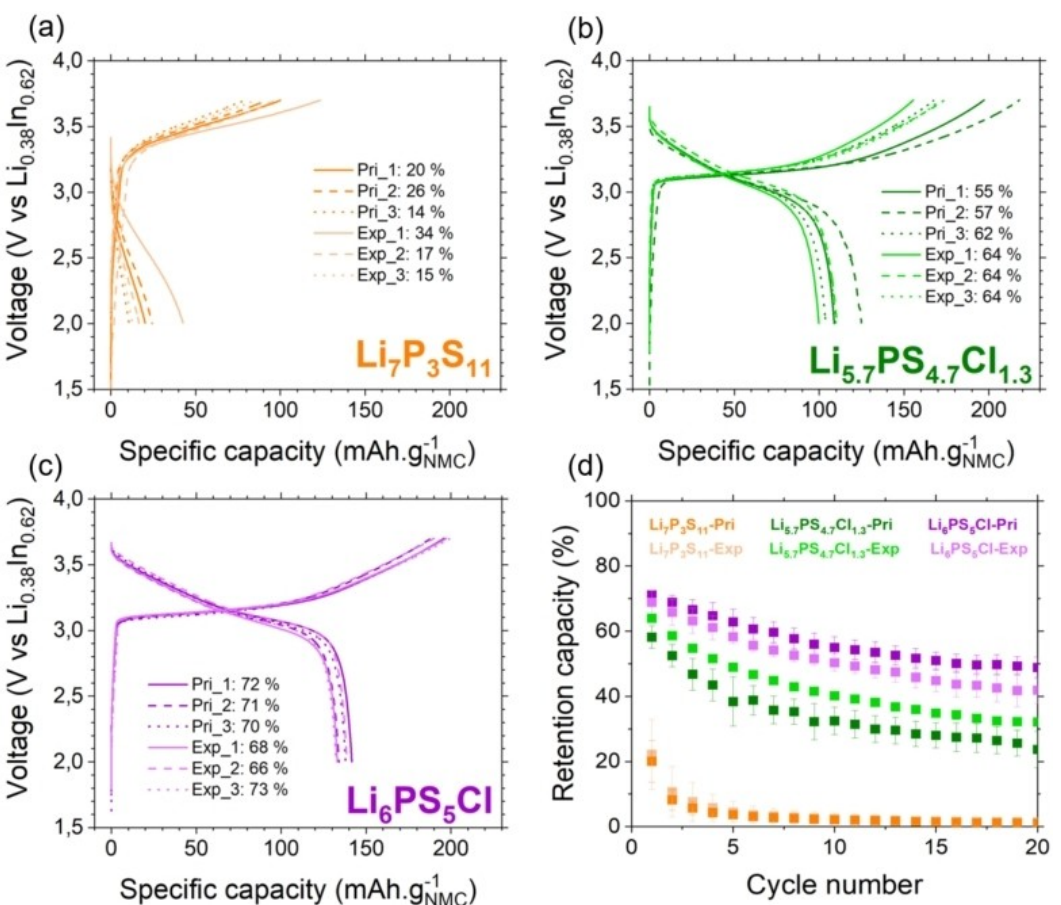


Figure 8. LiIn/SE/NMC cells cycling: a) 1st cycle based on $\text{Li}_7\text{P}_3\text{S}_{11}$ -Pri and $\text{Li}_7\text{P}_3\text{S}_{11}$ -Exp samples. b) 1st cycle based on $\text{Li}_{5.7}\text{PS}_{4.7}\text{Cl}_{1.3}$ -Pri and $\text{Li}_{5.7}\text{PS}_{4.7}\text{Cl}_{1.3}$ -Exp samples. c) 1st cycle based on $\text{Li}_6\text{PS}_5\text{Cl}$ -Pri and $\text{Li}_6\text{PS}_5\text{Cl}$ -Exp samples. d) Evolution of capacity retention with cycle number. $\text{Li}_7\text{P}_3\text{S}_{11}$ -Pri (dark orange), $\text{Li}_7\text{P}_3\text{S}_{11}$ -Exp (light orange), $\text{Li}_{5.7}\text{PS}_{4.7}\text{Cl}_{1.3}$ -Pri (dark green), $\text{Li}_{5.7}\text{PS}_{4.7}\text{Cl}_{1.3}$ -Exp (light green), $\text{Li}_6\text{PS}_5\text{Cl}$ -Pri (dark purple), $\text{Li}_6\text{PS}_5\text{Cl}$ -Exp (light purple). Three identical cells were tested in every case to assess reproducibility.

Conclusions

In this work, we studied *in-situ* the dynamics of H₂S emissions from three solid electrolytes, $\text{Li}_7\text{P}_3\text{S}_{11}$, $\text{Li}_{5.7}\text{PS}_{4.7}\text{Cl}_{1.3}$ and $\text{Li}_6\text{PS}_5\text{Cl}$, upon exposure to a dry room atmosphere at a dew point below -40°C, as well as the impact of trace levels of humidity on physico-chemical and electrochemical properties of the powders. Precise, real-time H₂S evolution profiles for the solid electrolytes were obtained thanks to the high sensitivity and fast response time of the OFCEAS measurement technique. We found that dynamics of H₂S emissions for both argyrodites $\text{Li}_{5.7}\text{PS}_{4.7}\text{Cl}_{1.3}$ and $\text{Li}_6\text{PS}_5\text{Cl}$ give rise to an initial peak of H₂S, which is above the recommended short-term exposure limit in the case of $\text{Li}_{5.5}\text{PS}_{4.5}\text{Cl}_{1.5}$, followed by a sharp decrease and stabilisation at low emission values, one order of magnitude below the 8-hour time weighted average (TWA) value. On the contrary, the same experiment carried out with $\text{Li}_7\text{P}_3\text{S}_{11}$ showed a slow rise of H₂S emissions in the first 30 min, followed by a stabilization at 2.5 ppm, just below the TWA. Pristine and exposed samples were then characterised by XRD, Raman spectroscopy and XPS. The most obvious change for exposed samples was observed by XPS, showing the presence of a Li_2CO_3

layer at the surface of both $\text{Li}_{6-x}\text{PS}_{5-x}\text{Cl}_{1+x}$ compounds. We think this lithium carbonate layer plays a passivation role for both argyrodites, significantly slowing the degradation of the material during the dry room exposure. This efficient passivation does not occur for $\text{Li}_7\text{P}_3\text{S}_{11}$ powder during the reaction with traces of humidity evidenced by H₂S release.

Subsequently, some electrochemical tests were run, comparing the performance of pristine and exposed samples. The ionic conductivity of the powders were checked first, and no significant impact was noticed for any of the powders. Finally, SSBs were assembled using pristine or exposed powders, in a LiIn/NMC configuration. The cell cycling revealed that $\text{Li}_7\text{P}_3\text{S}_{11}$ performed poorly in such cell, whether it was exposed to the dry room air or not. For $\text{Li}_{5.7}\text{PS}_{4.7}\text{Cl}_{1.3}$, the exposure to the dry room and formation of Li_2CO_3 layer seemed to have a small beneficial effect on the initial coulombic efficiency and a capacity retention. For $\text{Li}_6\text{PS}_5\text{Cl}$, the exposure to the dry room has slightly impacted the capacity retention of the cells.

Compared to previous studies tackling scale-up problematics of sulfide electrolytes, our work showed the particular dynamics of H₂S emission for three different sulfide solid electrolytes. We suggest that special care should be taken when

manipulating sulfide powders, and the initial peak of H₂S release observed for freshly-exposed argyrodite materials should be taken into account in risk assessments for the various steps of production of solid-state cells. The conditions we used for the exposure of SEs to the dry room atmosphere lead to observable changes in physico-chemical properties of the powder and electrochemical properties of associated cells. We are convinced that argyrodites are amongst the best solid electrolyte candidates for SSB technologies, and this work will provide additional information for the planning of scale-up projects.

Experimental Section

Pristine Li₇P₃S₁₁ sample (Li₇P₃S₁₁-Pri) was prepared using a mecano-synthesis route from Li₂S (99.98%, Sigma-Aldrich) and P₂S₅ (99%, Sigma-Aldrich) mixed in stoichiometric proportions to yield the global composition of Li₇P₃S₁₁. A premixing step was performed for 1 h in a Turbula, followed by a ball-milling step conducted for 15 g overall mass of mixed powders with 120 balls (Φ10 mm) in a jar (250 ml) made in yttria-stabilized zirconia. A Retsch PM-100 apparatus was used with a rotation speed fixed at 510 rpm for 16 h via intermittent millings (5 min / 5 min). The resulting powder was then annealed in an argon-filled quartz tube at 250 °C for 3 h. Pristine Li_{5.7}PS_{4.7}Cl_{1.3} sample (Li_{5.7}PS_{4.7}Cl_{1.3}-Pri) was also prepared using a mecano-synthesis route from Li₂S (99.98%, Sigma-Aldrich), P₂S₅ (99%, Sigma-Aldrich) and LiCl (99%, Sigma-Aldrich) mixed in stoichiometric proportions to yield the global composition of Li_{5.5}PS_{4.5}Cl_{1.5}. The ball-milling was conducted for 20 g overall mass of mixed powders with 130 balls (Φ10 mm) in a jar (250 mL) made in yttria-stabilized zirconia. A Retsch PM-100 apparatus was used with a rotation speed fixed at 380 rpm for 30 h via intermittent millings (5 min / 5 min). The resulting powder was then annealed in an argon-filled quartz tube at 550 °C for 5 h. The commercial grade of Li₆PS₅Cl sample was purchased from NEI (Li₆PS₅Cl-Pri).

Crystallographic phase identification was performed using a Bruker D8 Advanced diffractometer with Cu radiation ($\lambda_1 = 1.54056 \text{ \AA}$, $\lambda_2 = 1.54439 \text{ \AA}$). Kapton® tape was used to prevent samples from being exposed to air. Diffraction patterns were refined by Le Bail method using Fullprof software.

Raman spectroscopy was performed using an inVia Raman microscope from Renishaw with 532 nm laser excitation and < 0.2 mW power on the sample to prevent degradation. Sample preparation was performed in an argon-filled glovebox, where the powder samples were directly transferred and sealed inside a dedicated airtight optical cell. The window material was optical grade sapphire. The spectra were fitted using Origin with a Pseudo-Voigt function.

³¹P solid-state magic angle spinning NMR spectroscopy measurements were performed using a 11.7 T Bruker Avance III spectrometer operating at the Larmor frequency of 202.4 MHz. All samples were handled and packed in inserts disposed in zirconia rotor (Ø = 4 mm) in an Ar-filled glovebox. The spectra were obtained at a magic angle spinning rate of 8 kHz under pure nitrogen at room temperature. The acquisition sequence involved direct excitation using a 90° pulse length of 8.5 μs and recycling delay of 30 s. The spectrum was fitted using Origin with a Pseudo-Voigt function.

Samples were transferred directly from the glove box to the XPS spectrometer using a sealed transfer vessel to avoid exposure to air. XPS measurements were carried out with a Versaprobe II spectrometer from ULVAC-PHI using an X-ray source Al K α ($h\nu =$

1486.6 eV). All XPS measurements were carried out under ultrahigh vacuum conditions ($9 \times 10^{-8} \text{ Pa}$). The pass energy was set to 23.5 eV allowing an energy resolution of approximately 0.6 eV. The binding energy scale was calibrated on C 1s (adventitious carbon) at 284.8 eV. Curve fitting was accomplished using Multipak 9.9 software from ULVAC-PHI.

SEM was performed using a Sigma 300 from ZEISS located in dry room. A voltage of 1.5 keV was used with a secondary electrons detector (InLens). Image treatment was performed using Image J software.

For the gas measurements, 1 g of each pristine powder was weighted using a glass vial in a glove box filled with Ar ($\text{H}_2\text{O} < 0.1 \text{ ppm}$; $\text{O}_2 < 1 \text{ ppm}$), the vial was closed with a lid and sealed with tape before being transferred to the measurement setup in dry room ($\text{DP} = -40^\circ\text{C}$). The powder was then rapidly poured on the top of a 60 mm diameter coarse fritted disc in a 350 cm³ gas washing bottle (60 mm diameter, 210 mm height and 20 mm mouse opening) under a laboratory fume hood (aspiration capacity ~350 m³ h⁻¹) No additional manipulations with the powder was performed throughout the whole experiment after it was poured. Gas evolution measurement for the static powder was performed for 16 h, using a ProCeas® H₂S analyser (AP2E) based on infrared technology. The gases released by the SEs were pumped from the gas washing bottle using a diaphragm pump (with a flow of 21 mL min⁻¹) and analysed with high precision thanks to the OFCEAS principle.^[32] The advantages of this gas analyser are extremely high sensitivity, no interference with other molecules and independence of measurements on carrier gas and relative humidity (unlike majority of H₂S sensors^[12]). H₂S, SO₂ and H₂O were continuously monitored using two independent lasers, the data was recorded ones in a second. The LLOD were 1 ppb (vol) for H₂S and 5 ppb (vol) for SO₂. The higher limit of detection was 100 ppm (vol) for both H₂S and SO₂. Sulfinert®-treated stainless steel tubing and connections were used to avoid adsorption of gases along the gas lines. The gas measurement setup is presented in Figure 3(a) and details on a correlation between the capacitive dew point sensor data available in the dry room and the laser measurement are provided in Figure S7.

EIS was used to evaluate ionic conductivities for the SEs at room temperature. It was performed in the range between 1 Hz to 3 MHz using SP-50e potentiostat from Biologic®. Signal amplitude was fixed at 50 mV. The measurements were conducted at RT with 7 mm diameter pellet cold-pressed at 625 MPa (2 tons) along with two papyex® electrodes in a homemade airtight cell. The spectra were fitted using a Z Fit tool from EC-lab.

Solid-state cells were fabricated using 7 mm diameter home-made cells. A mixture of LiNi_{0.6}Mn_{0.2}Co_{0.2}O₂ (NMC₆₂₂, Targray), sulfide SE (pristine or exposed sample) and Vapor Grown Carbon Fiber (VGCF, Showa Denko) were ground in a mortar in the respective proportions 65/30/5 and 8.5 mg were used for the positive electrode composite. 40 mg of sulfide SE (pristine or exposed sample) were used for the separator and a Li_{0.38}In_{0.62}^[33] electrode was used as the negative electrode. The alloy negative electrode was obtained by co-lamination at room temperature of a lithium foil and an indium foil. The thickness of the foils were chosen to fit the target stoichiometry of the Li_{0.38}In_{0.62} alloy. Three identical cells were assembled with each sample to assess the reproducibility of the experiment. Cell preparation started with the densification of the SE at 128 MPa. In a second step, the positive electrode composite was added on one side of the densified SE and pressed at 255 MPa. The negative electrode was finally placed on the remaining side of the separator and the cell was closed under 80 MPa. The electrochemical investigation was performed at RT

using a VMP 3 from Biologic between 2.0 and 3.7 V vs. Li_{0.38}In_{0.62} and at C/20.

Supporting Information

Experimental details including ³¹P NMR and Raman spectra of Li_{5.7}PS_{4.7}Cl_{1.3}-Pri, the characterization of Pristine and Exposed samples (XRD with profile matching analysis, XPS spectra with Li 1s, S 2p and P 2p, SEM images), and the detailed tables displaying the fitted parameters for both XRD and EIS data (PDF). The authors have cited additional reference within the Supporting Information (Ref. [34]).

Acknowledgements

Authors are grateful to Prof. Claire Villevieille for providing the in-house SSB set-up.

Part of this work was carried out at the Platform for Nanocharacterisation (PFNC), CEA Grenoble, France.

Conflict of Interests

The authors declare that they have no conflict of interest.

Data Availability Statement

The data that support the findings of this study are available from the corresponding authors upon reasonable request.

Keywords: H₂S gas measurements • laser spectroscopy • photoelectron spectroscopy • dry room humidity • solid-state Li-ion batteries • sulfide solid electrolytes

- [1] a) H. Lee, P. Oh, J. Kim, H. Cha, S. Chae, S. Lee, J. Cho, *Adv. Mater.* **2019**, *31*, e1900376; b) X.-b. Cheng, R. Zhang, C.-z. Zhao, Q. Zhang, *Chem. Rev.* **2017**, *117*, 10403–10473; c) C. Wang, J. Liang, Y. Zhao, M. Zheng, X. Li, X. Sun, *Energy Environ. Sci.* **2021**, *14*, 2577–2619.
- [2] A. Varzi, R. Raccichini, S. Passerini, B. Scrosati, *J. Mater. Chem. A* **2016**, *4*, 17251–17259.
- [3] F. Mizuno, A. Hayashi, K. Tadanaga, M. Tatsumisago, *Electrochim. Solid-State Lett.* **2005**, *8*, 4–8.
- [4] H. J. Deisereth, S. T. Kong, H. Eckert, J. Vannahme, C. Reiner, T. Zaiss, M. Schlosser, *Angew. Chem. Int. Ed. Engl.* **2008**, *47*, 755–758.
- [5] a) Y. Seino, M. Nakagawa, M. Senga, H. Higuchi, K. Takada, T. Sasaki, *J. Mater. Chem. A* **2015**, *3*, 2756–2761; b) S. Boulineau, M. Courty, J. M. Tarascon, V. Viallet, *Solid State Ionics* **2012**, *221*, 1–5.
- [6] Y. Seino, T. Ota, K. Takada, A. Hayashi, M. Tatsumisago, *Energy Environ. Sci.* **2014**, *7*, 627–631.
- [7] L. Zhou, A. Assoud, Q. Zhang, X. Wu, L. F. Nazar, *J. Am. Chem. Soc.* **2019**, *141*, 19002–19013.
- [8] a) Y. G. Lee, S. Fujiki, C. Jung, N. Suzuki, N. Yashiro, R. Omoda, D. S. Ko, T. Shiratsuchi, T. Sugimoto, S. Ryu, J. H. Ku, T. Watanabe, Y. Park, Y. Aihara, D. Im, I. T. Han, *Nat. Energy* **2020**, *5*, 299–308; b) D. H. S. Tan, Y. T. Chen, H. Yang, W. Bao, B. Sreenarayanan, J. M. Doux, W. Li, B. Lu, S. Y. Ham, B. Sayahpour, J. Scharf, E. A. Wu, G. Deysher, H. E. Han, H. J. Hah, H. Jeong, J. B. Lee, Z. Chen, Y. S. Meng, *Science* **2021**, *373*, 1494–1499.
- [9] J. Lau, R. H. DeBlock, D. M. Butts, D. S. Ashby, C. S. Choi, B. S. Dunn, *Advanced Energy Materials* **2018**, *8*, 1800933.
- [10] H. Muramatsu, A. Hayashi, T. Ohtomo, S. Hama, M. Tatsumisago, *Solid State Ionics* **2011**, *182*, 116–119.
- [11] a) T. Ohtomo, A. Hayashi, M. Tatsumisago, K. Kawamoto, *J. Mater. Sci.* **2013**, *48*, 4137–4142; b) A. Hayashi, H. Muramatsu, T. Ohtomo, S. Hama, M. Tatsumisago, *J. Alloys Compd.* **2014**, *591*, 247–250; c) G. Liu, D. Xie, X. Wang, X. Yao, S. Chen, R. Xiao, H. Li, X. Xu, *Energy Storage Mater.* **2019**, *17*, 266–274; d) M. K. Tufail, L. Zhou, N. Ahmad, R. Chen, M. Faheem, L. Yang, W. Yang, *Chem. Eng. J.* **2021**, *407*, 127149–127149; e) M. Otoyama, K. Kuratani, H. Kobayashi, *RSC Adv.* **2021**, *11*, 38880–38888.
- [12] C. Singer, H.-C. Töpper, F. J. Günter, G. Reinhart, *Procedia CIRP* **2021**, *104*, 56–61.
- [13] S. Randau, D. A. Weber, O. Kötz, R. Koerver, P. Braun, A. Weber, E. Ivers-Tiffée, T. Adermann, J. Kulisch, W. G. Zeier, F. H. Richter, J. Janek, *Nat. Energy* **2020**, *5*, 259–270.
- [14] J. Schnell, H. Knörzer, A. J. Imbsweiler, G. Reinhart, *Energy Technol.* **2020**, *8*.
- [15] Y. J. Nam, D. Y. Oh, S. H. Jung, Y. S. Jung, *J. Power Sources* **2018**, *375*, 93–101.
- [16] M. R. Busche, D. A. Weber, Y. Schneider, C. Dietrich, S. Wenzel, T. Leichtweiss, D. Schröder, W. Zhang, H. Weigand, D. Walter, S. J. Sedlmaier, D. Houtarde, L. F. Nazar, J. Janek, *Chem. Mater.* **2016**, *28*, 6152–6165.
- [17] H. Yamane, M. Shibata, Y. Shimane, T. Junke, Y. Seino, S. Adams, K. Minami, A. Hayashi, M. Tatsumisago, *Solid State Ionics* **2007**, *178*, 1163–1167.
- [18] C. Dietrich, D. A. Weber, S. Culver, A. Senyshyn, S. J. Sedlmaier, S. Indris, J. Janek, W. G. Zeier, *Inorg. Chem.* **2017**, *56*, 6681–6687.
- [19] P. Adeli, J. D. Bazak, K. H. Park, I. Kochetkov, A. Huq, G. R. Goward, L. F. Nazar, *Angew. Chem. Int. Ed.* **2019**, *58*, 8681–8686.
- [20] H. Ott, *Phys. Zeitschrift* **1923**, *24*, 209–213.
- [21] X. Feng, P. H. Chien, Y. Wang, S. Patel, P. Wang, H. Liu, M. Immediato-Scuotto, Y. H. Yu, *Energy Storage Mater.* **2020**, *30*, 67–73.
- [22] a) K. Seol, C. Kaliyaperumal, A. Uthayakumar, I. Yoon, G. Lee, D. Shin, *Electrochim. Acta* **2023**, *441*; b) P. Lu, L. Liu, S. Wang, J. Xu, J. Peng, W. Yan, Q. Wang, H. Li, L. Chen, F. Wu, *Adv. Mater.* **2021**, *33*, e2100921.
- [23] Recommendation from the Scientific Committee on Occupational Exposure Limits for Hydrogen Sulphide (Ed.: E. Comission, SCOEL/SUM/124), **2007**.
- [24] X. Randrema, C. Barcha, M. Chakir, V. Viallet, M. Morcrette, *Solid State Sci.* **2021**, *118*, 106681–106681.
- [25] Y.-T. Chen, M. A. T. Marple, D. H. S. Tan, S.-Y. Ham, B. Sayahpour, W.-K. Li, H. Yang, J. B. Lee, H. J. Hah, E. A. Wu, J.-M. Doux, J. Jang, P. Ridley, A. Cronk, G. Deysher, Z. Chen, Y. S. Meng, *J. Mater. Chem. A* **2022**, *10*, 7155–7164.
- [26] J. Auvergniot, A. Cassel, D. Foix, V. Viallet, V. Seznec, R. Dedryvère, *Solid State Ionics* **2017**, *300*, 78–85.
- [27] a) N. V. Faenza, L. Bruce, Z. W. Lebens-Higgins, I. Plitz, N. Pereira, L. F. J. Piper, G. G. Amatucci, *J. Electrochem. Soc.* **2017**, *164*, A3727–A3741; b) N. Hornsveld, B. Put, W. M. M. Kessels, P. M. Vereecken, M. Creatore, *RSC Adv.* **2017**, *7*, 41359–41368; c) Y. You, H. Celio, J. Li, A. Dolocan, A. Manthiram, *Angew. Chem. Int. Ed.* **2018**, *57*, 6480–6485.
- [28] A. Gautam, M. Sadowski, N. Prinz, H. Eickhoff, N. Minafra, M. Ghidu, S. P. Culver, K. Albe, T. F. Fässler, M. Zobel, W. G. Zeier, *Chem. Mater.* **2019**, *31*, 10178–10185.
- [29] M. Calpa, N. C. Rosero-Navarro, A. Miura, K. Tadanaga, *Electrochim. Acta* **2019**, *296*, 473–480.
- [30] a) F. Hippauf, B. Schumm, S. Doerfler, H. Althues, S. Fujiki, T. Shiratsuchi, T. Tsujimura, Y. Aihara, S. Kaskel, *Energy Storage Mater.* **2019**, *21*, 390–398; b) D. Cao, X. Sun, Y. Li, A. Anderson, W. Lu, H. Zhu, *Adv. Mater.* **2022**, *34*, 1–15.
- [31] J. Auvergniot, A. Cassel, J.-B. Ledeuil, V. Viallet, V. Seznec, R. Dedryvère, *Chem. Mater.* **2017**, *29*, 3883–3890.
- [32] J. Morville, D. Romanni, M. Chenevier (University Joseph Fourier), WO 03/031949A1.
- [33] S. A. Webb, L. Baggetto, C. A. Bridges, G. M. Veith, *J. Power Sources* **2014**, *248*, 1105–1117.
- [34] R. Le Ruyet, R. Berthelot, E. Salager, P. Florian, B. Fleutot, R. Janot, *J. Phys. Chem. C* **2019**, *123*, 10756–10763.

Manuscript received: August 31, 2023

Revised manuscript received: October 26, 2023

Accepted manuscript online: November 3, 2023

Version of record online: November 22, 2023